Facile synthesis and characterization of magnetic iron oxide (Fe$_3$O$_4$)-loaded cationic amino-modified passion fruit shell nanocomposite and their application in removal of anionic Alizarin Red S dye from aqueous medium

Venkata Subbaiah Munagapati [a], Hsin-Yu Wen [b], Anjani R.K. Gollakota [c], Jet-Chau Wen [a,d,*], Kun-Yi Andrew Lin [e,f,**], Chi-Min Shu [d], Vijaya Yarramuthi [g], Praveen Kumar Basivi [h], Chang Woo Kim [i], Jeung-Tai Tang [j]

[a] Research Centre for Soil & Water Resources and Natural Disaster Prevention (SWAN), National Yunlin University of Science and Technology, Douliu, Yunlin 64002, Taiwan
[b] Department of Pathology, West China Hospital, Sichuan University, Chengdu 610041, PR China
[c] Department of Chemical and Materials Engineering, National Yunlin University of Science and Technology, Douliu, Yunlin 64002, Taiwan
[d] Department of Safety, Health, and Environmental Engineering, National Yunlin University of Science and Technology, Douliu, Yunlin 64002, Taiwan
[e] Department of Environmental Engineering & Innovation and Development Center of Sustainable Agriculture, National Chung Hsing University, Taichung, Taiwan
[f] Institute of Analytical and Environmental Sciences, National Tsing Hua University, Hsinchu, Taiwan
[g] Department of Chemistry, Vikrama Simhapuri University, Nellore 524320, Andhra Pradesh, India
[h] Pukyong National University Industry-University Cooperation Foundation, Pukyong National University, Busan 48513, Republic of Korea
[i] Department of Nanotechnology Engineering, College of Engineering, Pukyong National University, Busan 48513, Republic of Korea
[j] Department of Information & Management, National Yunlin University of Science and Technology, Douliu, Yunlin 64002, Taiwan

ARTICLE INFO

ABSTRACT

A newly synthesized magnetic nanocomposite, iron oxide-loaded cationic amino-modified passion fruit shell (Fe$_3$O$_4$@CMPFS), was utilized as a sorbent to eliminate anionic Alizarin Red S (ARS) dye from the wastewater. The Fe$_3$O$_4$@CMPFS was characterized to confirm the properties by physicochemical methods such as VSM, XRD, pH$_{PZC}$, BET, FTIR, and FE-SEM with EDX. Batch tests were conducted to study the adsorption process, focusing on factors like the solution pH (from 2.0 to 11), amount of Fe$_3$O$_4$@CMPFS (from 10 to 80 mg/30 mL), contact duration (from 0 to 240 min), agitation speed (from 0 to 400 rpm) and temperature (from 298 to 328 K). The optimal conditions for attaining a 92.3 % removal efficiency were found to be a pH of 2.0, 60 mg of Fe$_3$O$_4$@CMPFS, a contact time of 60 min, agitation at 250 rpm, and a temperature of 298 K. The Fe$_3$O$_4$@CMPFS was determined to have a pH$_{PZC}$ value of approximately 6.2. The kinetic data indicated that the adsorption of ARS onto Fe$_3$O$_4$@CMPFS followed the pseudo-second-order model (high R^2 = 0.9919; low SSE = 1.5) and was governed by film and intraparticle diffusion mechanisms. Furthermore, the isotherm data fit well with the Langmuir model (high R^2 = 0.9983; low χ^2 = 12.69), suggesting monolayer adsorption behaviour. The maximal sorption uptake of ARS on the Fe$_3$O$_4$@CMPFS was determined to be 233.4 ± 3.174 mg/g at 298 K through the Langmuir model. The estimated $\Delta H°$ (18.3 kJ/mol) and $\Delta S°$ (82 J/mol K) indicate the endothermic and enhanced randomness at the adsorbent/solute interface. The negative $\Delta G°$ values (−6.2298 to −8.7283 kJ/mol at 298–328 K) confirm spontaneous sorption dominated by physisorption. The Fe$_3$O$_4$@CMPFS composite had good recyclability and was easy to separate from water, which maintained excellent adsorption performance after eight regeneration cycles. The superb adsorption efficiency and recycling performance of Fe$_3$O$_4$@CMPFS provide a prospect way to remove ARS dye from industrial effluents.

* Corresponding author at: Research Centre for Soil & Water Resources and Natural Disaster Prevention (SWAN), National Yunlin University of Science and Technology, Douliu, Yunlin 64002, Taiwan.
** Corresponding author at: Department of Environmental Engineering & Innovation and Development Center of Sustainable Agriculture, National Chung Hsing University, Taichung, Taiwan.
E-mail addresses: wenjc@yuntech.edu.tw (J.-C. Wen), linky@nchu.edu.tw (K.-Y.A. Lin).

1. Introduction

The expansion of industrial activities, coupled with population growth, has led to significant degradation of aquatic ecosystems. Textile industries, known for their high water consumption, produce substantial quantities of wastewater, contributing to the deterioration of water quality in surface water bodies [1]. Due to lenient enforcement of environmental regulations, many of these industries discharge untreated effluents into surface water bodies, leading to decreased water transparency and adverse effects on aquatic life, including reduced photosynthesis and increased mortality rates [1]. Alizarin Red S, which is a water-soluble anthraquinone dye frequently utilized in textiles for its staining properties, presents a considerable challenge due to its resistance to degradation. ARS contains aromatic rings that confer high thermal, physicochemical stability, and optical, making it difficult to break down through conventional methods. Consequently, the discharge of untreated wastewater containing ARS into the environment has health implications due to its toxicity and potential to cause cancer [2]. Given these challenges, there is a pressing need to develop efficient and eco-friendly methods for removing ARS from wastewater before its released into natural water sources like rivers and lakes.

Several approaches for eliminating dyes from wastewater have been created, including chemical, physical, and biological methods. These include ozonation [3,4], photocatalytic degradation [5], membrane separation [6], coagulation/flocculation [7,8], mineralization [9], oxidation [10], electrochemical filtration [11], etc. However, every technology has its own limitations in terms of effectiveness, environmentally friendly processing, and cost control, which can prevent the achievement of desirable results. On the other hand, adsorption presents itself as a feasible approach for treating wastewater, outperforming other purification methods because of its straightforward process for a wide range of pollutants and its cost efficiency. Moreover, the adsorption process averts the generation of toxic byproducts associated with the degradation of complex organic molecules. Recent research endeavours have primarily centred on the utilization of natural adsorbents as alternatives to conventional ones, driven by environmental and economic considerations. Although activated carbon has historically served as a prevalent adsorbent, its utilization has been impeded by cost considerations compared to alternative options. Many researchers have investigated low-cost agricultural wastes such as pomegranate peel [12], barberry stem [13], moringa seeds [14], banana peel [15], watermelon rind [16], sugarcane bagasse [17], etc., as biosorbents for the elimination of dyes from polluted water solutions. These materials are favoured for their affordability, widespread availability, and eco-friendly nature.

Passion fruit (*Passiflora edulis*) is a high-value subtropical fruit characterized by its distinctive purple or yellow peel. A notable by-product of passion fruit processing is passion fruit peel residue, which lacks economic value and frequently presents challenges for environmentally sound disposal. By utilizing passion fruit peel as a low-cost adsorbent, the economic value of this agricultural by-product can be enhanced, concurrently mitigating waste disposal costs. The utilization of agricultural waste materials in their natural state as adsorbents is subject to certain limitations, including the leaching of plant-soluble constituents into treated water, diffusion constraints leading to reduced adsorption uptake, low surface area, and inadequate disposal of the treated biosorbent [18,19]. To address these constraints, various modifications such as surface functionalization, activation, and impregnation with specific chemicals or reagents have been proposed. These modifications aim to introduce functional groups or enhance surface properties, thereby improving the adsorption performance of the adsorbents. These modifications target the introduction of functional groups and the enhancement of surface properties, thereby boosting the adsorption performance of the adsorbents. For example, surface functionalization with groups such as amino (—NH$_2$), carboxyl (—COOH), or hydroxyl (—OH) can enhance the affinity of the adsorbent for dye

molecules through specific chemical interactions like π-π stacking interaction, electrostatic attraction, and H-bonding. Numerous studies have reported dye elimination using modified agro wastes, for instance, SMDRS [20], QAMOPP [21], QPPAC [22], β-cyclodextrin modified pine cone powder [23], trimellitic-modified pineapple peel [24], etc.

The integration of nanoparticles such as zinc oxide, titanium dioxide, iron oxides, and carbon nanotubes into modified agro-based adsorbents imparts ferromagnetic properties to these materials. This modification facilitates the rapid and efficient separation of the biosorbent from water solutions following the sorption process. The challenge of separating the biosorbent from the aqueous medium can be effectively mitigated by developing magnetically modified biosorbents. Magnetic separation is acknowledged as a rapid, efficient, and cost-effective technique applicable to both large- and small-scale wastewater treatment operations. As a result, magnetic composites incorporating an agro-industrial residue matrix emerge as a viable alternative for contaminant removal. Among the various magnetic materials available magnetic (Fe$_3$O$_4$) is particularly noteworthy due to its widespread use in contaminant adsorption. Its magnetic properties, low cost, environmentally benign nature, and capacity to treat large volumes of wastewater make magnetite an attractive choice for this application. Various magnetically modified agro wastes such as magnetized orange peel waste [25], magnetite nanoparticles loaded fig leave [26], lotus leaf powder@iron oxide [27], magnetic Fe$_3$O$_4$ loaded papaya seed powder [28], magnetic ion modified with sky fruit [29], PKSAC-Fe$_3$O$_4$ [30], etc. were effectively used as sorbents and presented outstanding sorption uptake of dyes.

The novelty of this study is developing and characterizing a novel Fe$_3$O$_4$@CMPFS as a highly efficient biosorbent for the ARS dye elimination from contaminated wastewater. No researcher has ever used or investigated this adsorbent for ARS dye removal. As a result, the study presents a fresh and efficient adsorbent for treating ARS in contaminated water. It demonstrates its exceptional performance and ability to be reused, highlighting its potential for removing ARS dye. This study offers an innovative approach to water purification by introducing a unique adsorbent with unparalleled efficiency, reusability, and adaptability in addressing ARS pollutants.
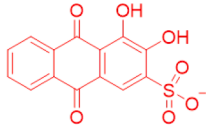
Currently, numerous methods have been utilized and examined for the production of iron oxide nanoparticles, including hydrothermal synthesis, microemulsion, co-precipitation, and thermal decomposition. Co-precipitation, in particular, is a simple method for synthesizing iron oxides from aqueous solutions. In this study, we used the co-precipitation technique to synthesize the Fe$_3$O$_4$@CMPFS nanocomposite. The prepared Fe$_3$O$_4$@CMPFS composite was then characterized and employed as a biosorbent to eliminate ARS from aqueous environments. The impacts of various factors, such as shaking time, amount of Fe$_3$O$_4$@CMPFS, solution pH, temperature, and stirring speed, on the adsorption of Fe$_3$O$_4$@CMPFS for ARS were studied. The adsorption mechanism, kinetic, isotherm, and thermodynamic variables were also examined. The adsorption–desorption properties of the composite were evaluated to determine the Fe$_3$O$_4$@CMPFS's reusability.

2. Materials and methods

2.1. Chemicals

All chemical reagents, including diethylenetriamine (C$_4$H$_{13}$N$_3$), sodium hydroxide (NaOH), Alizarin Red S dye (Table 1 presents the chemical structure and characteristics of the ARS), ferrous sulfate heptahydrate (FeSO$_4$·7H$_2$O), epichlorohydrin (C$_3$H$_5$ClO), hydrochloric acid (HCl), and iron(III) chloride hexahydrate (FeCl$_3$·6H$_2$O) were bought from Sigma-Aldrich (USA). The substances were all of analytical quality and were utilized without additional refinement. Deionized (DI) water was employed throughout the tests.

Table 1

General characteristics of the ARS dye.

Chemical structure	
Molecular formula	$C_{14}H_7NaO_7S$
IUPAC name	3,4-Dihydroxy-9,10-dioxo-9,10-dihydroanthracene-2-sulfonic acid
Class	Anthraquinone
CI Number	58,005
Molecular weight (g/mol)	360.28
Form	Powder
Absorption, λ_{max}	423 nm

2.2. ARS stock solution

A solution of ARS at a concentration of 1000 mg/L was prepared by combining 0.25 g of the dye with 1000 mL of DI water. Subsequently, this solution was thinned to the necessary concentration for various experimental purposes.

2.3. Synthesis of Fe₃O₄@CMPFS nanocomposite

Passion fruits were acquired from a local market, and their outer shells were removed. They were sliced, rinsed with DI water to remove dust and other impurities, sun-dried for five days, and then subjected to 343 K heat overnight to eliminate moisture. After that, they were ground in a mill to get fine powder. Next, the resulting powder was rinsed multiple times with hot DI water to eliminate colour and turbidity. Finally, the cleaned material was dried in an oven at 353 K overnight and sifted through a 0.35 mm sieve. The resulting powder was named PFS.

The previously reported method was used to modify PFS. The procedure involved mixing 150 mL of 1.25 M NaOH with 100 mL of C_3H_5ClO at 303 K. Afterward, the solution was stirred with 10.0 g of the PFS for 40 min at 313 K. Several rinses were performed until the resulting substance reached a pH of 7. The substance was then dried in an oven at 343 K. Subsequently, the dried materials were agitated with a mixture of 150 mL of 0.125 M NaOH and 25 mL of $C_4H_{13}N_3$ solution. The resulting mixtures were manually stirred at 343 K for 50 min before being washed with DI water to achieve a pH of 7.0. Finally, the washed powder was dried in an oven at 343 K for 3 h, resulting in the production of cationic amino-modified passion fruit shell (CMPFS) powder.

Fe₃O₄@CMPFS was synthesized via the chemical coprecipitation method. Initially, a mixture of 12 g of $FeSO_4\cdot7H_2O$ and 6.0 g of $FeCl_3\cdot6H_2O$ was stirred in 500 mL of DI water in a beaker. The stirring continued at 343 K for 2 h. Subsequently, 10 g of CMPFS was added while stirring constantly for 30 min, followed by the addition of (5 M) NaOH solution to achieve a pH of 11. The colour of the combination turned from dark brown to black, indicating the creation of a magnetic composite. After cooling, a magnet was used to test the solution, confirming its attraction and, thus, the formation of the magnetic composite. The mixture was then centrifuged at 7000 rpm for 8 min, and the remaining material was cleaned with excess DI water until the pH reached 7.0. The remaining residue underwent centrifugation once again, then was subjected to 4 h of drying in an oven at 343 K. Afterward, it was crushed into a powdery substance and filtered through a 0.350 mm mesh to create the Fe₃O₄-loaded CMPFS composite, named the Fe₃O₄@CMPFS.

2.4. Analytical methods

The Fe₃O₄@CMPFS crystal structure was examined using a D8 Advance X-ray Diffractometer (XRD) from Germany. The instrument employed a CuKα radiation with a wavelength of 1.5405 Å, operated at 40 mA, 40.0 kV, and a scanned rate of 0.2/min for line broadening profile analysis and phase consistency evaluation. Field Emission Scanning Electron Microscopy (FESEM) with an Energy Dispersive X-ray (EDX) spectroscopy (JEOL; JSM-7610FPlus; Japan) was utilized to assess the structural morphology and elemental composition of Fe₃O₄-CMPFS and ARS-loaded Fe₃O₄@CMPFS. Prior to imaging, the particles were coated with gold, and an accelerating voltage of 20.0 kV was applied. The textural features of Fe₃O₄@CMPFS were evaluated using a Quantachrome BET surface area analyzer (USA) through N_2 adsorption/desorption testing at 77.3 K. Prior to analysis, the substances were degassed at 393 K for 6 h. The Brunauer-Emmett-Teller (BET) and Barrett-Joyner-Halenda (BJH) methodologies were utilized to assess the pore radius, pore volume, and surface area correspondingly. The magnetic characteristics of Fe₃O₄-CMPFS were examined using a Vibrating Sample Magnetometer (VSM) from Lakeshore, USA, at ±20 kOe and 25 °C. The functional groups of Fe₃O₄@CMPFS and ARS-loaded Fe₃O₄@CMPFS were analyzed using a Thermo Nicolet iS10 Fourier Transform Infrared (FTIR) spectrophotometer (USA). The images were scanned in the wavelength range of 4000–400 cm^{-1} using KBr-pellets to improve the signal to noise ratio.

2.5. Point of zero charge (pHₚZC) of Fe₃O₄-CMPFS

The pH_{PZC} was measured using the solid-addition technique [31]. In short, (0.01 M) NaCl solution in 50 mL polypropylene tubes was adjusted to pH values ranging from 2.0 to 11 ($pH_{initial}$) using 0.1 M of NaOH and HCl. Various tubes were each supplemented with 60 mg of Fe₃O₄-CMPFS and placed in an incubator at 298 K with an agitation of 250 rpm. After 48 h, the pH of the samples was measured (pH_{final}) using a Mettler Roledo Secen Easy pH tester (USA), and the results were graphed against the initial pH ($pH_{initial}$). The pH_{PZC} is indicated by the $pH_{initial}$ at which the change in pH is zero.

2.6. Optimization of adsorption parameters

Prior to conducting isotherms, kinetics, and thermodynamic modeling, this study also requires optimization of the adsorption process using a batch method to determine the optimal conditions for ARS adsorption on the Fe₃O₄@CMPFS surface. In this optimization investigation, the impact of pH was examined using a magnetic Fe₃O₄@CMPFS at a quantity of 60 mg with pH variations ranging from 2 to 11. The pH levels for every variant were adjusted using 0.1 M of HCl (or) NaOH solutions. The mass of the Fe₃O₄@CMPFS composite was optimized by varying the dosage from 10 to 80 mg. The contact duration was adjusted to a range of 0–240 min. The agitation speed was optimized in multiples of 0–400 rpm. The influence of temperature was anlayzed starting at 298, 308, 318, and 328 K. The optimization of all parameters was investigated using an ARS solution of 50 mg/L with a volume of 30 mL. Following the adsorption process, the Fe₃O₄@CMPFS is separated using an external magnet, and the remaining ARS in the sample is measured using a Jasco V750 model Ultraviolet–Visible spectrophotometer (Japan) at a λ_{max} of 423 nm. Finally, the adsorption uptake (q_e) and the removal efficiency (*R%*) were calculated from Eqs. (1) and (2).

$$q_e = \frac{(C_o - C_e)V}{M} \tag{1}$$

$$R\% = \left(\frac{C_o - C_e}{C_o}\right) \times 100\% \tag{2}$$

in the above equations, M (g) is the Fe₃O₄@CMPFS weight, and V (mL) indicates the ARS solution volume. C_e (mg/L) and C_o (mg/L) are the equilibrium and starting ARS concentrations, respectively.

2.7. Reusability studies

The ability of Fe$_3$O$_4$@CMPFS to be reused was evaluated through multiple adsorption and desorption cycles. 30 mL of 50.0 mg/L ARS solution was treated with 60 mg of Fe$_3$O$_4$@CMPFS until adsorption equilibrium was reached. Using an external magnet, the ARS-loaded Fe$_3$O$_4$@CMPFS was separated from the solution and then regenerated using various desorbing eluents (0.1 M HCl/Methanol, 0.1 M NaOH, 0.1 M NaOH/Ethanol, 0.1 M NaOH/Methanol, 0.1 M HCl, 0.1 M HCl/Ethanol, Acetone, Ethanol, and Methanol). The regenerated Fe$_3$O$_4$@CMPFS composite was agitated for 60 min at 298 K with an agitation speed of 250 rpm, then rinsed with DI water until reaching a pH level of 7, and ultimately dried in an oven at 343 K until a constant weight was attained. The desorbed Fe$_3$O$_4$@CMPFS was then weighed and used for the subsequent adsorption cycle. This process was frequent eight times to determine the reusability of the Fe$_3$O$_4$@CMPFS.

2.8. Error analysis

All ARS batch adsorption experiment was conducted as a triplicate independent sample, and error bars representing average values with standard deviations (less than 5 %) were used to depict all of the experimental results. The following equations were used to calculate the sum of the square (SSE) and chi-square (χ^2) values, which were used to assess whether kinetic and isotherm models best suit the data.

$$SSE = \frac{\sqrt{\sum(q_{e,cal} - q_{e,exp})^2}}{N} \tag{3}$$

$$\chi^2 = \sum \frac{\left(q_{e,exp} - q_{e,cal}\right)^2}{q_{e,exp}} \tag{4}$$

In the equations, $q_{e,cal}$ and $q_{e,exp}$ represent the calculated and experimental uptakes (mg/g), respectively, and N denotes the number of experimental data points.

3. Results and discussion

3.1. Fe$_3$O$_4$@CMPFS characterization

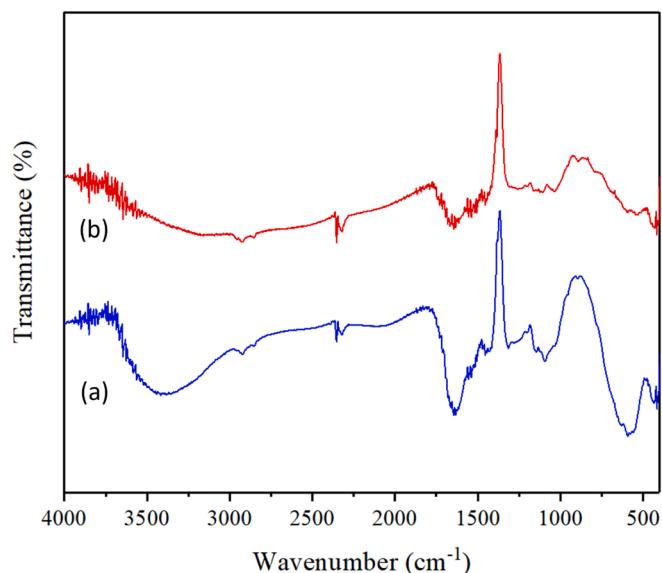A closer insight into the presence of different functional groups on

Fig. 1. FTIR spectrum of (a) Fe$_3$O$_4$@CMPFS and (b) ARS-loaded Fe$_3$O$_4$@CMPFS.

the surface of Fe$_3$O$_4$@CMPFS and ARS-loaded Fe$_3$O$_4$@CMPFS was analyzed by FTIR spectra displayed in Fig. 1. In the spectra of Fe$_3$O$_4$@CMPFS (Fig. 1(a)), the band approximately 3413 cm^{-1} corresponds to amine (NH) and hydroxyl (OH) stretching as well as the intramolecular hydrogen bonds [32]. The peaks at 2927 and 2850 cm^{-1} are related to the asymmetric stretching and bending vibrations of the CH groups in —CH$_2$, and —CH$_3$, respectively [33]. The band at 1635 cm^{-1} is attributed to the C=O stretching in the aromatic ring [34]. The peak observed at 1454 cm^{-1} could be assigned to the bending vibrations of the methoxy group [35]. The band 1313 cm^{-1} is a result of the C—H bending vibration of the alkyl group [36]. The band at 1146 cm^{-1} is attributed to the C—O—C stretching vibrations and indicates the existence of lignin, cellulose, and hemicellulose [37]. The band at 1091 cm^{-1} is associated with the C—O stretching vibration of the primary alcohol group [38]. An intense band at 589 cm^{-1} is attributed to the Fe—O stretching vibrations [39], confirming the successful formation of Fe$_3$O$_4$ nanoparticles on the surfaces of the Fe$_3$O$_4$@CMPFS. After the adsorption of ARS (Fig. 1(b)), the peaks at 3413, 2927, 2850, 1635, 1454, 1146, 1091, and 589 cm^{-1} were slightly shifted to 3174, 2924, 2848, 1644, 1452, 1160, 1031, and 537 cm^{-1} due to the ARS adsorption on the Fe$_3$O$_4$@CMPFS surface.

The FE-SEM and EDX techniques were used to evaluate the morphological characteristics and surface properties of the Fe$_3$O$_4$@CMPFS composite both before and after the adsorption of ARS dye. At a magnification of ×2000, Fig. 2a shows the FE-SEM image revealing Fe$_3$O$_4$@CMPFS had a porous, rough, and irregular surface having agglomerated particles. In Fig. 2b, the FE-SEM image at the same magnification displays a morphological change in the Fe$_3$O$_4$@CMPFS after the ARS adsorption as a result of the dye accumulation on the surface. A closer analysis of the FE-SEM image of ARS-loaded Fe$_3$O$_4$@CMPFS revealed a smoother surface compared to Fe$_3$O$_4$@CMPFS, with reduced porosity. This suggests that the ARS dye has been adsorbed onto the pores of Fe$_3$O$_4$@CMPFS. The EDX analysis of the Fe$_3$O$_4$@CMPFS composite was used to measure the elemental composition before and after sorption. The EDX spectrum of Fe$_3$O$_4$@CMPFS (Fig. 2c) shows the presence of elements C, O, Na, S, Mg, K, Cl, Ca, and Fe. A distinct Fe peak is observed in the EDX spectrum of Fe$_3$O$_4$@CMPFS, indicating the successful deposition of Fe$_3$O$_4$ nanoparticles on the CAMPFS surface. After the adsorption (as shown in Fig. 2d), noticeable changes in the elemental compositions were observed, confirming that ARS has effectively adhered to the surface of the Fe$_3$O$_4$@CMPFS.

The VSM was used to analyze the magnetic properties of Fe$_3$O$_4$@CMPFS in a magnetic field ranging from ±20 kOe at 298 K. At magnetic ambient temperature, the internal hysteresis loop of Fe$_3$O$_4$@CMPFS displayed an 'S' shaped plot (see Fig. 3). The material's S-shaped magnetization curve indicates superparamagnetic behaviour [40]. The Ms (saturation magnetization) of Fe$_3$O$_4$@CMPFS was determined to be 31.7 emu/g, confirming its sufficient magnetic properties to be attracted by an exterior magnetic field.

The Fe$_3$O$_4$@CMPFS adsorption and desorption isotherm was measured at 77.4 K, as displayed in Fig. S1(a), in order to assess the surface characteristics of Fe$_3$O$_4$@CMPFS. The identified adsorption type was type IV with an H$_3$ hysteresis loop, typically indicating a mesoporous structure as per IUPAC guidelines, suggesting the presence of ample slit pores and mesoporosity [41]. Using the BJH method, the pore volume and surface area were determined to be 0.238 cc/g and 115.5 m^2/g, respectively, as illustrated in Fig. S1(b). Furthermore, a distinct peak for D_p (pore size distribution) occurred at 2.7 nm, and the D_p range was found to be 2.1–47 nm, falling within the mesoporous structure range (2–50 nm) as per the BJH method. The mesoporous structure of Fe$_3$O$_4$@CMPFS exhibited effective ARS from wastewater due to its substantial pore volume and surface area.

The nanocomposite's crystalline structure was examined through XRD analysis. The XRD pattern of Fe$_3$O$_4$@CMPFS is illustrated in Fig. S2. The main distinct peaks observed at 2θ values of 74.3°, 62.8°, 57.1°,
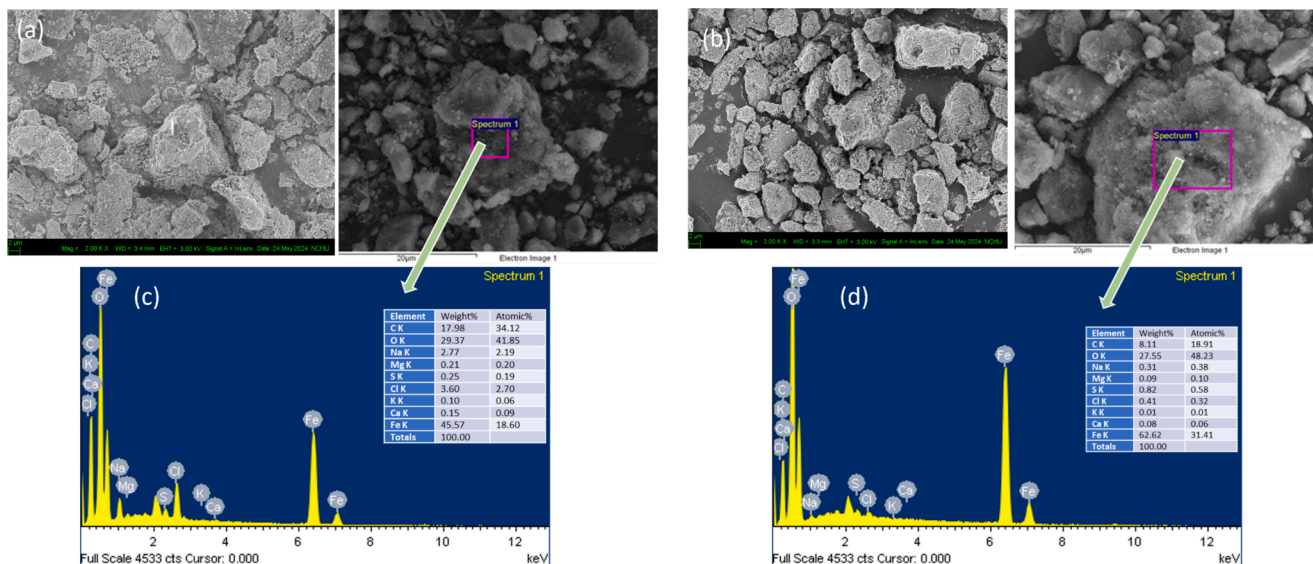
Fig. 2. SEM image of (a) Fe$_3$O$_4$@CMPFS and (b) ARS-loaded Fe$_3$O$_4$@CMPFS; EDX image of (c) Fe$_3$O$_4$@CMPFS, and (d) ARS-loaded Fe$_3$O$_4$@CMPFS.
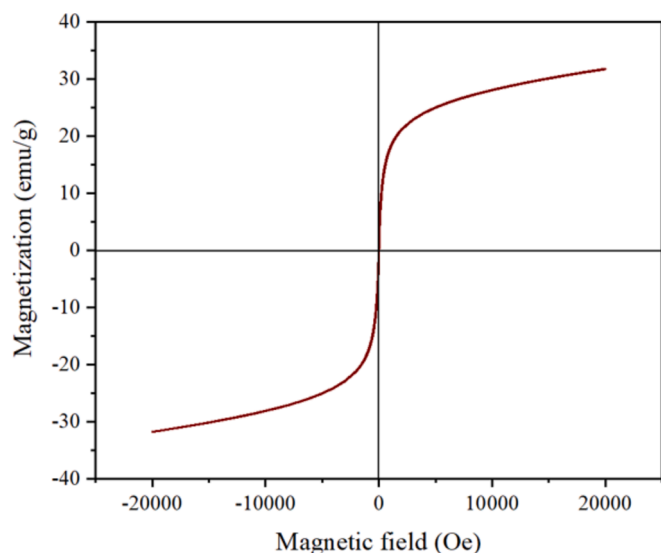

Fig. 3. Magnetic hysteresis loop of the synthesized Fe$_3$O$_4$@CMPFS.

53.8°, 43.2°, 35.6°, and 30.1°, which corresponded to the crystal planes of 533, 440, 511, 422, 400, 311, and 220, respectively. The Fe$_3$O$_4$@CMPFS diffraction peaks are consistent with the inverse cubic spinel structure of magnetic iron oxide (Fe$_3$O$_4$) nanoparticles (JCPDS File No: 19-0629). The result confirms that the magnetic Fe$_3$O$_4$ nanoparticles were perfectly incorporated on the CMPFS surface.

3.2. Point of zero charge (pH$_{PZC}$) of Fe$_3$O$_4$@CMPFS

The pH$_{PZC}$, or isoelectric point, is the point at which the positive charges on the Fe$_3$O$_4$@CMPFS surface are balanced by the negative charges, resulting in a neutral charge. According to Fig. 4(a), the pH$_{PZC}$ of Fe$_3$O$_4$@CMPFS is 6.2. As a result, in solutions with a pH below 6.2, the Fe$_3$O$_4$@CMPFS surface will become protonated due to an excess of H$^+$ (protons), which enhances the adsorption of negatively charged molecules or anions (Fig. 4(b)). If the pH of the solution is above 6.2, the Fe$_3$O$_4$@CMPFS functional groups will lack H$^+$ due to OH$^-$, resulting in a negative charge on the Fe$_3$O$_4$@CMPFS surface and promoting the sorption of molecules with a positive charge or cations (Fig. 4(c)). Given that ARS carries a negative charge, pH values below 6.2 are anticipated to facilitate the adsorption between the negatively charged dye molecules and the positively charged Fe$_3$O$_4$@CMPFS surface.
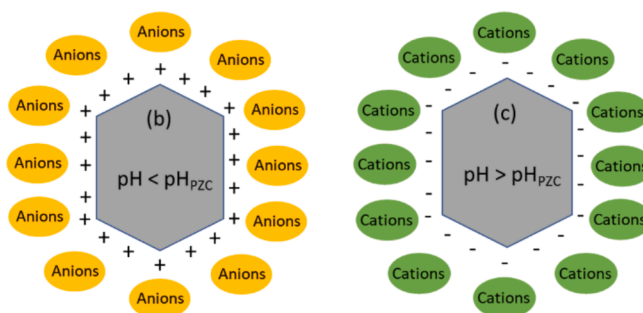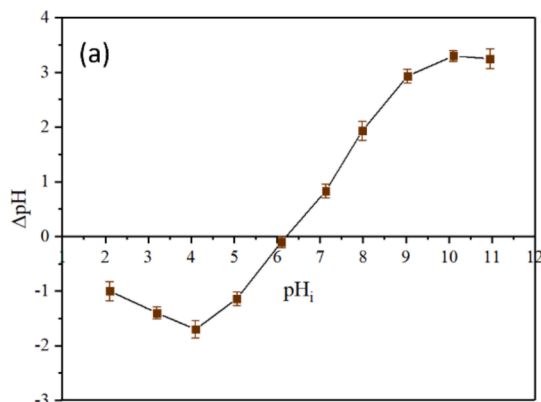

Fig. 4. Mechanism for dye adsorption as a function of point of zero charge (pH$_{PZC}$) (a) pH$_{PZC}$ of Fe$_3$O$_4$@CMPFS, (b) when pH < pH$_{PZC}$ and (c) when pH > pH$_{PZC}$.

3.3. Influence of pH

The solution pH is important because of the ionization of functional groups in adsorbate molecules and the charge on the adsorbent surface. Depending on the solution pH, the functional groups in the dye molecule and adsorbent surface may become deprotonated or protonated, influencing the electrostatic forces between the biosorbent and dye. The influence of pH on the adsorption of ARS dye on Fe$_3$O$_4$@CMPFS nanocomposite was examined within a pH range of 2.0–11, as proved in Fig. 5(a). The maximal adsorption uptake and efficiency were found to be 45.4 mg/g and 92.3 %, respectively, at pH 2.0. Based on Fig. 5(a), it was observed that ARS adsorption is more efficient under acidic conditions compared to basic environments because excessive positive charges accumulate at lower pH levels. At low pH values, the —NH$_2$ and —OH functional groups in the Fe$_3$O$_4$@CMPFS undergo protonation to form —NH$_3^+$ and —OH$_2^+$, leading to the creation of positive surface charges on Fe$_3$O$_4$@CMPFS. As the ARS possessed a sulfonic acid group, it was negatively charged in the aqueous solution. Consequently, there was a strong electrostatic contact between the positively charged surface of Fe$_3$O$_4$@CMPFS and ARS (Fig. 6). As the pH increased and became more alkaline, the surface charge of Fe$_3$O$_4$@CMPFS became negative, resulting in greater electrostatic repulsion with ARS molecules (Fig. 6). Furthermore, the competitive adsorption of hydroxides (OH$^-$) also contributed to a decrease in adsorption and removal performance. Similar behaviour has been observed in the removal of ARS using various adsorbents [1,42,43].

3.4. Effect of Fe$_3$O$_4$@CMPFS mass

The quantity of adsorbent used has a significant effect on adsorption processes. The impact of the quantity of biosorbent on the removal of ARS dye with Fe$_3$O$_4$@CMPFS was tested at various adsorbent amounts ranging from 10 to 80 mg/30 mL, as depicted in Fig. 5(b). It was noticed that the % of dye removal increased quickly when the adsorbent dosage was between 10 mg and 40 mg, followed by a slower increase from 50 to 80 mg. The heightened percentage of dye sorption with a rise in the amount of adsorbent can be attributed to the greater adsorption sites and a more forceful driving effect [44]. In Fig. 5(b), it is evident that there was no significant change in the dye removal percentage beyond the 60 mg dose, as all the adsorption active sites in Fe$_3$O$_4$@CMPFS were already taken. Therefore, 60 mg was chosen as the optimal adsorbent dosage. On the other hand, the amount of ARS adsorbed on Fe$_3$O$_4$@CMPFS decreased from 81.3 to 17.5 mg/g as the Fe$_3$O$_4$@CMPFS dose was raised from 10 to 80 mg. This decrease might be attributed to a greater surface area at lower adsorption doses, resulting in more collisions between particles of biosorbent mass at a constant dye concentration and volume, leading to the saturation of active sites. Additionally, interactions such as the formation of aggregates at higher adsorbent doses could decrease the adsorption uptake due to the reduction in total biosorbent surface areas and the length of the diffusion path [45,46].
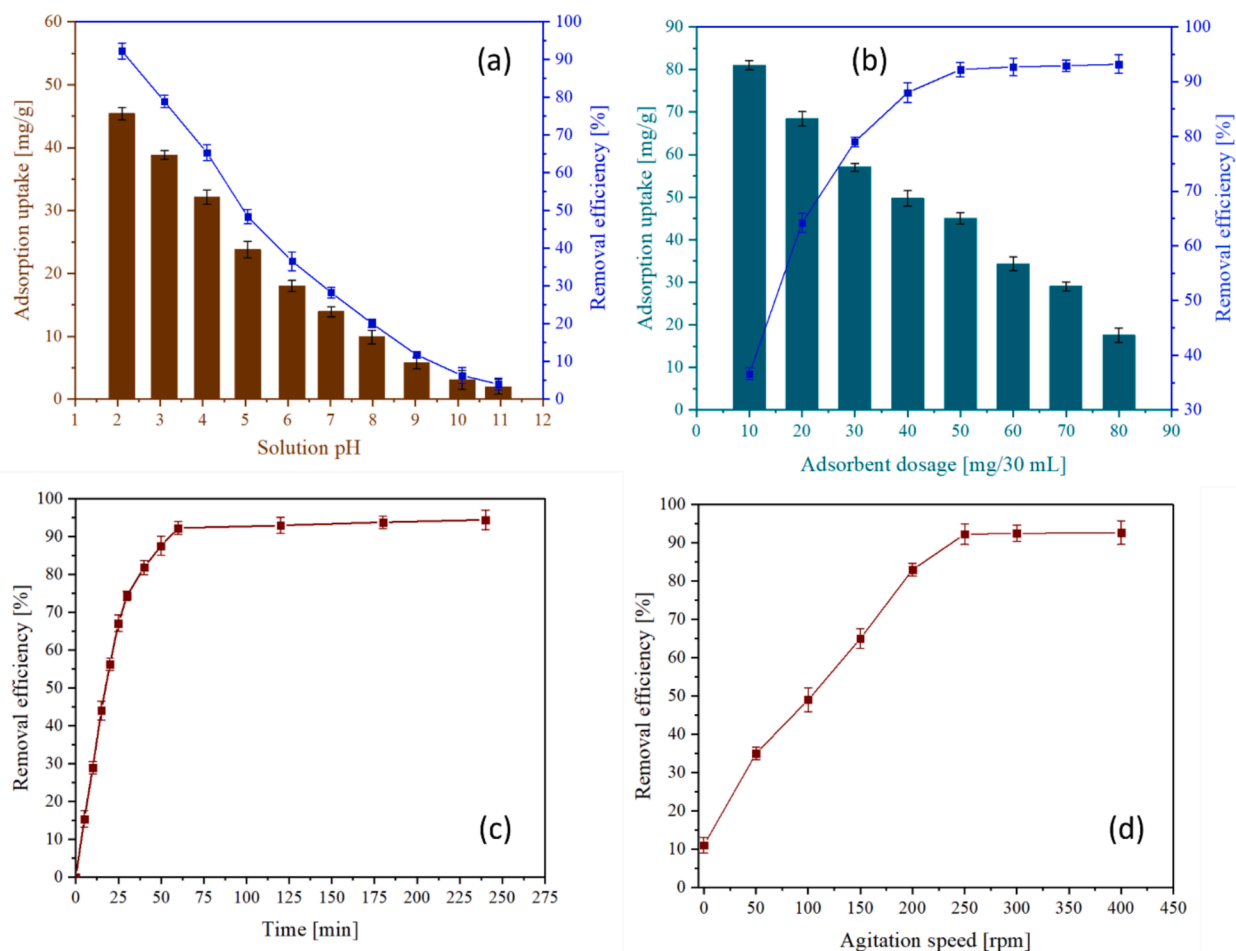

Fig. 5. Effect of (a) pH solution [C$_o$ = 50 mg/L; V = 30 mL; M = 60 mg; T = 298 K; t = 60 min; speed = 250 rpm, pH = 2.0–11], (b) dosage [C$_o$ = 50 mg/L; V = 30 mL; pH = 2.0; T = 298 K; t = 60 min; speed = 250 rpm, dosage = 10–80 mg/30 mL], (c) agitation speed [C$_o$ = 50 mg/L; M = 60 mg; V = 30 mL; pH = 2.0; T = 298 K; t = 60 min; speed = 0–400 rpm], and (d) contact time [C$_o$ = 50 mg/L; M = 60 mg; V = 30 mL; pH = 2.0; T = 298 K; speed = 250 rpm; t = 0–240 min] on the removal of ARS by Fe$_3$O$_4$@CMPFS.
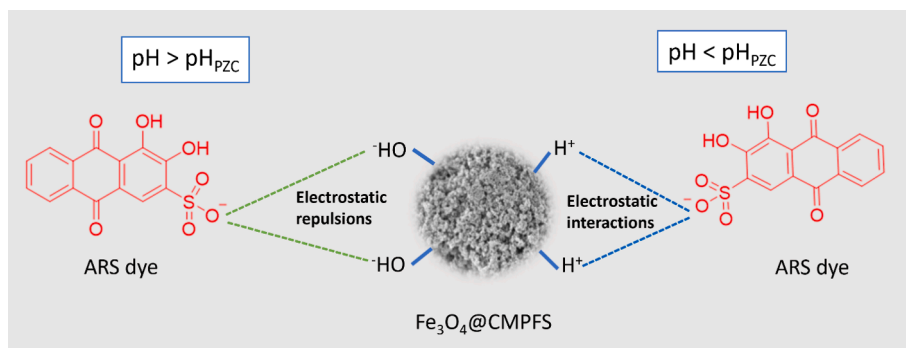
Fig. 6. The possible interaction mechanism between the ARS dye and Fe$_3$O$_4$@CMPFS.

3.5. Effect of contact duration

The duration of contact plays a critical role in the effective use of adsorbents in practical applications, with rapid adsorption being a desirable trait. The influence of contact duration on the sorption of ARS onto Fe$_3$O$_4$@CMPFS composite is illustrated in Fig. 5(c). The removal efficiency notably rose as the contact time increased. Most of the ARS dye was adsorbed during the initial contact periods. After 60 min, the adsorption of ARS dye on Fe$_3$O$_4$@CMPFS slowed down, and further increases in contact time did not result in a higher percentage of dye removal. The initially high removal efficiency may be due to the abundance of available empty sites on the adsorbent during the initial stages of adsorption. However, as time progressed, the vacant adsorbent sites became saturated with ARS dye molecules, leading to a decrease in the number of available active sites [47]. The findings indicate that 92.3 % of the ARS dye adsorption occurred within 60 min. Therefore, 60 min has been identified as the optimal contact period for the adsorption tests.

3.6. Effect of stirring speed

The speed of stirring during the sorption process has an impact on the rate at which the dye is adsorbed onto the biosorbent. Additionally, the mass transfer coefficient is increased in the bulk dye solution due to the creation of an external boundary layer as a result of solute distribution caused by the agitation rate. Fig. 5(d) illustrates the effect of stirring speed (0–400 rpm) on the efficiency of ARS sorption onto Fe$_3$O$_4$@CMPFS. The results indicated that the removal efficiency rose from 11.3 to 92.5 % as the speed grew from 0 to 250 rpm. This improvement is due to several factors. Accelerating the agitation process can prevent agglomeration, thereby reducing the surface area available for adsorption by the adsorbent particles. Another benefit is the reduction of resistance in the boundary layer surrounding the adsorbent particles, which may hinder their migration to the sorption sites. Increasing the agitation speed can enhance the interaction between the biosorbent and adsorbate by promoting a greater number of collisions [48]. Furthermore, the findings demonstrated that the removal efficiency remained consistent at speeds exceeding 250 rpm, suggesting that further increasing the agitation speed did not result in perceptible benefits. Therefore, the agitation speed of 250 rpm was chosen for the adsorption study of ARS.

3.7. Adsorption kinetics

An examination of the adsorption kinetics was carried out to gain a comprehensive understanding of the sorption processes of ARS dye and to effectively assess the performance of the Fe$_3$O$_4$@CMPFS composite. To achieve this, the sorption kinetic data of ARS were analyzed using PFO (pseudo-first-order)and PSO (pseudo-second-order) kinetic models. The non-linearized PFO and PSO models can be represented by the following equations:

$$q_t = q_{e1}(1 - e^{-k_1 t}) \tag{5}$$

$$q_t = \frac{q_{e2}^2 k_2 t}{1 + q_{e2} k_2 t} \tag{6}$$

where q$_t$ adsorbed ARS quantity at time t, q$_{e1}$ and q$_{e2}$ (mg/g) are the equilibrium ARS amounts adsorbed into the adsorbent mass, respectively. The adsorption rate constants are represented as k$_1$ (min^{-1}) and k$_2$ (g/mg min), respectively. Fig. 7(a) illustrates the experimental data and the fitted plots of the PFO and PSO models. The obtained kinetic variables and constants are listed in Table 2. The PSO kinetic model exhibits a high correlation coefficient (R^2 = 0.9919) and low error (SSE = 1.5) value for ARS dye adsorption compared to the PFO model (R^2 = 0.9601, SSE = 3.33). Furthermore, the calculated q$_e$ value (47.17 mg/g) from the PSO model matches the experimental q$_e$ value (46.52 mg/g), indicating that ARS adsorption onto Fe$_3$O$_4$@CMPFS follows a PSO kinetic model. Accordingly, it can also be concluded that chemisorption could also be incorporated to control the adsorption mechanism.

3.7.1. Intraparticle diffusion model

The proposed model by Weber and Morris was used to examine the diffusion mechanism of the ARS in Fe$_3$O$_4$@CMPFS. This model is known as the intraparticle diffusion (IPD) model and is represented by the following Eq. (7):

$$q_t = k_{id}t^{0.5} + C \tag{7}$$

where k$_{id}$ (mg/g min) is the IPD rate constant, and C is the boundary layer thickness constant, which can be obtained from Fig. 7(b). The plot shows multiple linear sections, indicating that the adsorption process is influenced by more than one step. Based on Table 3, the diffusion rate constants follow the sequence k$_{id,1}$ > k$_{id,2}$ > k$_{id,3}$, demonstrating that the first step represents the instantaneous diffusion phase, during which a large number of dye molecules are quickly adsorbed to the fresh active sites of Fe$_3$O$_4$@CMPFS. After nearly all the external active sites are occupied, the dye molecules enter the adsorbent pores and adhere to the interior surfaces of the pores, where the IPD is involved in the process (second stage). Lastly, the very small value of the IPD rate constant in the third stage indicates that equilibrium is being approached. Additionally, the linear curves do not pass through the origin, suggesting that the sorption kinetics may be simultaneously influenced by IPD and film diffusion [49].

3.8. Adsorption isotherms

The models for isotherms illustrate how the adsorbent and dye interact and are crucial in determining adsorption uptake, optimizing adsorbent consumption, and designing a suitable sorption system. As a result, four commonly used models (Temkin, Langmuir, Dubinin-Radushkevich, and Freundlich) were utilized in the isotherm study to
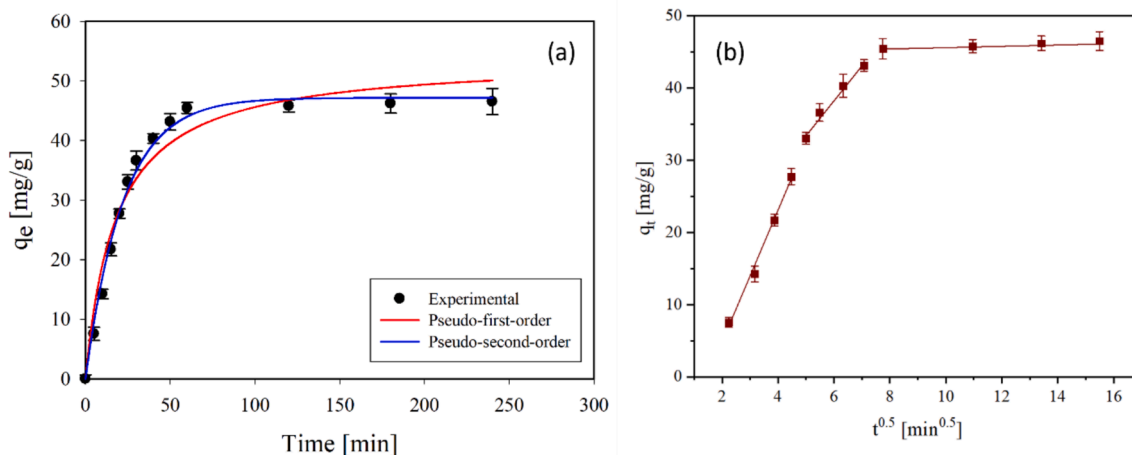
Fig. 7. (a) Adsorption kinetic plots [C_o = 50 mg/L; M = 60 mg; V = 30 mL; pH = 2.0; T = 298 K; speed = 250 rpm] and (b) Intraparticle diffusion model for the adsorption of ARS onto Fe_3O_4@CMPFS.

Table 2
The kinetic parameters of the adsorption of ARS onto the Fe_3O_4@CMPFS at 298 K.

Kinetic model	Parameter	Value
Pseudo-first-order	$q_{e,\,exp}$ (mg/g)	46.52
	$q_{e1,\,cal}$ (mg/g)	53.82 ± 2.564
	k_1 (1/min)	0.0450 ± 0.001
	R^2	0.9601
	SSE	3.33
Pseudo-second-order	$q_{e2,\,cal}$ (mg/g)	47.17 ± 0.796
	k_2 (g/mg min)	0.0010 ± 0.0002
	R^2	0.9919
	SSE	1.5

Table 3
Parameters of the intraparticle diffusion model for the adsorption of ARS onto the Fe_3O_4@CMPFS.

Stages	Parameter	Value
I	$K_{id,1}$ (mg/g min$^{0.5}$)	9.0919 ± 0.576
	C_1 (mg/g)	9.9443 ± 2.859
	R^2	0.9921
	SSE	0.9599
II	$K_{id,2}$ (mg/g min$^{0.5}$)	4.7466 ± 0.475
	C_2 (mg/g)	13.443 ± 2.036
	R^2	0.9804
	SSE	0.7542
Equilirbium	$K_{id,3}$ (mg/g min$^{0.5}$)	0.1407 ± 0.0093
	C_3 (mg/g)	44.315 ± 0.114
	R^2	0.9914
	SSE	0.0536

gain a deeper understanding of the sorption mechanism and to determine the interaction between ARS dye and Fe_3O_4@CMPF composite.

The Langmuir model explains how a single layer of molecules attaches to a surface with a set amount of active sites without any interaction between the attached molecules on neighboring active sites. The Langmuir isotherm can be mathematically represented in a non-linear form as follows:

$$q_e = \frac{q_{max}K_LC_e}{1 + K_LC_e} \tag{8}$$

where K_L, C_e, and q_{max} represent the Langmuir constant relevant to the energy of adsorption (L/mg), the equilibrium concentration of ARS dye (mg/L), and the sorption uptake (mg/g), respectively. Also, the Langmuir separation coefficient, R_L, is calculated by the following Eq. (9):

$$R_L = 1/(1 + K_LC_o) \tag{9}$$

The value of R_L predicts which type of sorption characteristics belong to one of the following four types: unfavourable sorption ($R_L > 1.0$), linear sorption ($R_L = 1.0$), irreversible sorption ($R_L = 0$), and favourable sorption ($0 < R_L < 1.0$).

The Freundlich isotherm suggests that adsorption occurs through multilayer sorption on a heterogeneous surface, which can be expressed by the following Eq. (10):

$$q_e = K_fC_e^{1/n} \tag{10}$$

where K_f represents the Freundlich isotherm constant (in mg/g), which indicates the binding energy, and n is a sorption intensity. The value of $1/n$ signifies whether the sorption is favourable ($1.0 > 1/n > 0$), unfavourable ($1.0 < 1/n$), or irreversible ($1/n = 1.0$).

The Dubinin-Radushkevich (D-R) isotherm can be used to estimate the porosity of the adsorbent and the heterogeneity of energies on its surface. This can be mathematically expressed as

$$q_e = q_mexp(-K\varepsilon^2) \tag{11}$$

where K (mol^2/J^2) is the sorption coefficient's mean free energy, and ε is the Polanyi potential, which is obtained from Eq. (12):

$$\varepsilon = RTln\left(1 + \frac{1}{C_e}\right) \tag{12}$$

where R denotes the gas constant in J/mol K, and T denotes the temperature. The mean free energy E (kJ/mol) per molecule of adsorbate during its transfer from the solution to the solid surface can be computed using Eq. (13):

$$E = 1/\sqrt{2K} \tag{13}$$

The value of E reflects the adsorption mechanism by this attachment to some extent: ion exchange (16.0 kJ/mol > E ≥ 8.0 kJ/mol), chemisorption (16.0 kJ/mol ≤ E) and physisorption (8.0 kJ/mol > E).

The Temkin isotherm states that the heat of adsorption decreases in a linear fashion as the adsorption process takes place, which is due to the increased interaction between the biosorbent and the adsorbate. This linear relationship is defined by the following equation:

$$q_e = BlnK_T + BlnC_e \tag{14}$$

where K_T (L/g) is the Temkin equilibrium binding constant, and B (J/mol) is the Temkin constant related to the heat of sorption.

Fig. 8 exhibits the fitting curves of D-R, Langmuir, Temkin, and Freundlich isotherms, along with the variables for the isotherm models which are detailed in Table 4. As per the table, the Langmuir model exhibited a higher non-linear correlation coefficient ($R^2 = 0.9983$) and lower Chi-square error values of ($\chi^2 = 12.69$) compared to the Freundlich ($R^2 = 0.9531$, $\chi^2 = 345.73$), D-R ($R^2 = 0.8075$, $\chi^2 = 960.19$), and Temkin ($R^2 = 0.9861$, $\chi^2 = 69.32$) isotherm models. This suggests that the Langmuir model provides a better fit for the equilibrium sorption data, confirming homogeneous surface with monolayer sorption of ARS onto Fe$_3$O$_4$@CMPF. The adsorption uptake (q_{max}) of Fe$_3$O$_4$@CMPF was determined as 233.4 ± 3.174 mg/g, and the calculated value of R_L was below 1 (0.04), again confirming the favourable adsorption of ARS dye onto the Fe$_3$O$_4$@CMPF. The value of 1/n in the Freundlich model was found to be 0.272 ± 0.042, further indicating the favourable adsorption of ARS onto the Fe$_3$O$_4$@CMPF. The mean free energy E calculated from the D-R model (Eq. (13)) was found to be 6.41 ± 0.095 kJ/mol, which is <8.0 kJ/mol. Hence, it can thus be concluded that physisorption played a dominant role in the adsorption of ARS onto Fe$_3$O$_4$@CMPF. The Temkin isotherm shows that the equilibrium binding constant K_T is 0.8573 ± 0.049 L/g, indicating the highest binding energy. On the other hand, the value of the constant B is 58.043 ± 0.248 J/mol, signifying the heat of adsorption for ARS onto Fe$_3$O$_4$@CMPF.

3.9. Comparison of results

The Fe$_3$O$_4$@CMPF composite's adsorption uptake for ARS removal was compared to various other adsorbents in Table 5 from previous literature [1,2,50–59]. It was observed that the Fe$_3$O$_4$@CMPF composite exhibited a higher adsorption uptake compared to other biosorbents. The increased sorption uptake was attributed to the presence of active functional groups like amine and hydroxyl, which facilitate the adsorption of anionic ARS dye molecules. Additionally, this adsorbent system is cost-effective and easy to prepare. Therefore, Fe$_3$O$_4$@CMPF is a favourable option for wastewater treatment.

3.10. Temperature effect

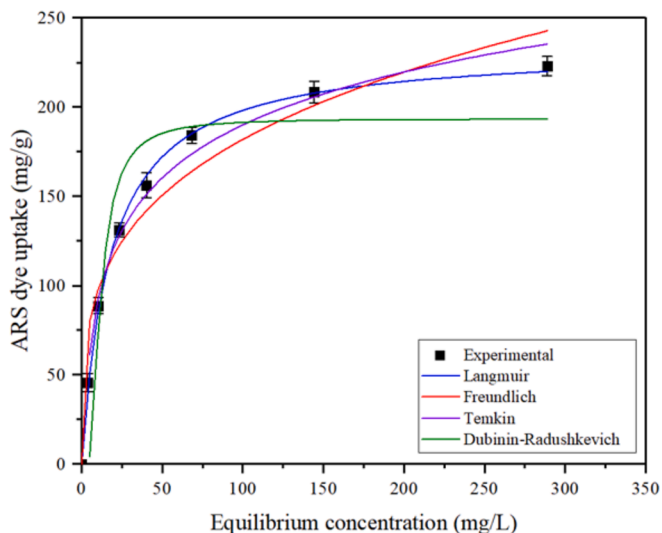The efficiency of the adsorbent in adsorption is significantly affected

Fig. 8. Non-linear isotherms plots for adsorption of ARS onto Fe$_3$O$_4$@CMPFS [C$_o$ = 50–500 mg/L; M = 60 mg; V = 30 mL; pH = 2.0; T = 298 K; t = 60 min; speed = 250 rpm].

Table 4
The isotherm parameters of the adsorption of ARS onto the Fe$_3$O$_4$@CMPFS at 298 K.

Isotherm model	Parameter	Value
Langmuir	q_{max} (mg/g)	233.4 ± 3.174
	K_L (L/mg)	0.0562 ± 0.003
	R^2	0.9983
	χ^2	12.69
Freundlich	K_f (mg/g)	51.97 ± 10.259
	1/n	0.272 ± 0.042
	R^2	0.9531
	χ^2	345.73
Dubinin-Radushkevich	q_m (mg/g)	193.51 ± 14.407
	K (mol^2/J^2)	0.0122 ± 0.000007
	E (kJ/mol)	6.41 ± 0.095
	R^2	0.8075
	χ^2	960.19
Temkin	B (J/mol)	58.043 ± 0.248
	K_T (L/mg)	0.8573 ± 0.049
	R^2	0.9861
	χ^2	69.32

by the temperature of the solution. As a result, a sequence of tests was conducted to study the impact of temperature on the % removal of ARS onto Fe$_3$O$_4$@CMPFS. According to Fig. S3(a), it was noted that the removal % of ARS dye rose from 92.3 to 96.4 % as the temperature escalated from 298 to 328 K. The rise in the removal % of ARS as the temperature rose suggests that the sorption process is endothermic. The high removal efficiency at higher temperatures can be attributed to the raised diffusion of the dye molecules due to the more excellent kinetic energy present at elevated temperatures [60]. The adsorption of ARS onto Fe$_3$O$_4$@CMPFS is more favourable at high temperatures.

3.11. Adsorption thermodynamics and activation energy

The study of thermodynamics yields significant information about how changes in temperature affect the process of adsorption. The following equations were used to estimate the associated parameters, including Gibbs free energy change ($\Delta G°$), entropy change ($\Delta S°$), and enthalpy change ($\Delta H°$).

$$\Delta G^o = \Delta H^o - T\Delta S^o \tag{15}$$

$$\Delta G^o = -RTlnK_d \tag{16}$$

$$K_d = \frac{q_e}{C_e}$$
$$= \frac{\text{Amount of ARS dye adsorbed onto Fe}_3\text{O}_4\text{@CMPFS at equilibrium}}{\text{ARS dye equilibrium concentration}} \tag{17}$$

$$lnK_d = -[\Delta H^o/RT] + [\Delta S^o/R] \tag{18}$$

$$\Delta S^o = \frac{\Delta H^o - \Delta G^o}{T} \tag{19}$$

where T indicates the solution temperature, R (8.314 J/mol K) is the gas constant, and K_d represents the distribution constant respectively. By plotting ln K_d vs. 1/T a straight line is found as depicted in Fig. S3(b). The $\Delta S°$ and $\Delta H°$ were acquired from the slope and intercept of the fitted line, respectively. The values for the thermodynamics parameters of ARS are listed in Table 6. The parameter $\Delta G°$ determines whether spontaneous adsorption occurs. If $\Delta G°$ is negative, it means adsorption is spontaneous; if it is positive, it indicates a non-spontaneous process. The values of $\Delta G°$ at 298, 308, 318, and 328 K from Table 6 show that all

Table 5

Comparison of Fe$_3$O$_4$@CMPFS with other adsorbents for ARS adsorption.

Adsorbent	pH	Dosage	Temp.	Time	q_{max} (mg/g)	Reference
Fe$_2$O$_3$@BC-KC composite	2.0	0.25 (g)	318	90	174.9	[1]
NiFe$_2$O$_4$/polyaniline magnetic composite	NA	0.03 g	303	90	186	[2]
SSZ-13	3.0	0.03	298	120	210.75	[50]
Fe$_3$O$_4$@PPy NPs	4–5.4	0.1–0.12 g	298	60	116.3	[51]
Magnetic talc (Fe$_3$O$_4$@Talc) nanocomposite	3.0	0.05 g	293	60	11.76	[52]
Fe$_3$O$_4$@NiO core–shell magnetic nanoparticles	3.0	3.0 g	288	90	223.3	[53]
Polyetheleneimine-functionalized magnetic carbon nanotubes	6.0	NA	298	40	196.08	[54]
activated carbon/γ-Fe$_2$O$_3$ nano-composite	2.0	0.01 g	NA	60	108.7	[55]
APTES grafted silica	2.0	NA	NA	40	59.8	[56]
Multi-walled carbon nanotubes (MWCNT)	2.0	NA	318	100	135.2	[57]
Chitosan-clay composite	2.0	0.05 g	328	10	44.39	[58]
Zinc oxide nanoparticles	4.0	0.4	303	35	123.3	[59]
Iron oxide-loaded cationic amino-modified passion fruit shell (Fe$_3$O$_4$@CMPFS)	2.0	0.06 g	298	60	233.4 ± 3.174	Present study

NA: Not available.

Table 6

Thermodynamic parameters for the adsorption of ARS onto Fe$_3$O$_4$@CMPFS at different temperatures.

Temperature [K]	Thermodynamic parameters				
	$\Delta G°$ (kJ/mol)	$\Delta S°$ (J/mol K)	$\Delta H°$ (kJ/mol)	S*	E$_a$
298	−6.2298				
308	−7.0448	82	18.3	0.055	20.4
318	−7.7999				
328	−8.7283				

these values were negative and decreased with rising temperature, suggesting that the adsorption of ARS was spontaneous and became more favourable at higher temperatures [61]. In general, the computed $\Delta G°$ values can indicate whether an adsorption process is a chemisorption (for $-400 < \Delta G° < -80$ kJ/mol) or physisorption (for $-20 < \Delta G° < 0$ kJ/mol) [62]. With $\Delta G°$ values from −6.2298 to −8.7283 kJ/mol, falling between −20 and 0 kJ/mol, a physisorption mechanism is suggested, indicating an electrostatic force between the adsorption sites and the adsorbing ion. The $\Delta S°$ represents the rate of change of randomness in the adsorption process. A positive $\Delta S°$ signifies a rise in disorder at the solid–liquid interface during the adsorption of ARS molecules [63]. The ARS sorption process is deemed endothermic due to the positive $\Delta H°$ value of 18.3 kJ/mol. The magnitude of $\Delta H°$ is a key indicator for distinguishing between chemical and physical adsorption. Typically, the heat released during physisorption falls within the 2.1–20.9 kJ/mol range, while the heat of chemisorption falls within the 20.9–418.4 kJ/mol [64]. With a calculated $\Delta H°$ value falling within the range of 2.10–20.9 kJ/mol, it suggests that the ARS adsorption onto the Fe$_3$O$_4$@CMPFS was physical.

The experimental data was utilized to estimate the activation energy (E_a) and sticking probability (S*) to provide additional evidence that physisorption is the primary mechanism. These values were determined by applying a modified Arrhenius equation that is associated with surface coverage (θ) as follows:

$$S^* = (1 - \theta)e^{-E_a/RT} \tag{20}$$

$$lnS^* = ln(1 - \theta) - E_a/RT \tag{21}$$

$$ln(1 - \theta) = lnS^* + E_a/RT \tag{22}$$

The value of the S* in the adsorption of ARS dye by Fe$_3$O$_4$@CMPFS composite was between 0 and 1. S* represents a temperature-dependent system function that indicates the adsorbate's entry into the intraparticle space after coming into contact with the adsorbent surface [65]. The following equation can be used to get the surface coverage (θ):

$$\theta = [1 - C_e/C_o] \tag{23}$$

The values of the E_a and S* were obtained from a plot of $1/T$ vs. ln (1 − θ) (Fig. S3(c)), respectively, and they are listed in Table 6. The magnitude of E_a provides insight into the nature of adsorption, whether it is predominantly chemical or physical. Typically, chemisorption involves E_a in the range of 40–800 kJ/mol, while physisorption is associated with a relatively lower E_a of 5–40 kJ/mol [62]. The E_a for the adsorption of ARS falls within the range of 5–40 kJ/mol, indicating a low potential energy barrier. This suggests that the adsorption of ARS on the Fe$_3$O$_4$@CMPFS is primarily driven by physisorption.

3.12. Regeneration of Fe$_3$O$_4$@CMPFS

An effective adsorbent should demonstrate the ability to be reused, in addition to having a high adsorption capacity and rapid adsorption rate for practical applications. To achieve this, various desorbing eluents, such as 0.1 M NaOH, 0.1 M NaOH/Ethanol, 0.1 M NaOH/Methanol, 0.1 M HCl, 0.1 M HCl/Ethanol, 0.1 M HCl/Methanol, Acetone, Ethanol, and Methanol, were studied for removing ARS adsorbed on the Fe$_3$O$_4$@CMPFS composite. Experimental findings indicated that the removal efficiency after the first regeneration with the aforementioned desorbing eluents was 92.5 %, 86.7 %, 69.1 %, 28.3 %, 59.8 %, 47.2 %, 61.6 %, 72.4 %, and 55.2 %, respectively. This suggests that the 0.1 M NaOH solution could be selected as the optimal desorbing eluent. The reusability cycles were conducted up to eight times, and the adsorption efficiencies of the regenerated Fe$_3$O$_4$@CMPFS for ARS were calculated. The adsorption efficiency of the Fe$_3$O$_4$@CMPFS reduced gradually as the number of regeneration cycles increased. This decline can be ascribed to the reduction of surface characteristics and functional groups on the adsorbent's surface, leading to a decrease in active sorption sites. Nonetheless, the outcomes illustrated in Fig. S4 suggest that the adsorption removal efficiency of ARS remained above 77.9 % after eight cycles of regeneration, indicating that the magnetic Fe$_3$O$_4$@CMPFS composite exhibits good reusability and stability.

3.13. ARS dye removal from water samples

The efficacy of Fe$_3$O$_4$@CMPFS in removing ARS dye from different water samples was evaluated. Adsorption experiments were conducted using 60 mg of Fe$_3$O$_4$@CMPFS in 30 mL of a 50 mg/L ARS dye solution prepared with various water samples at 298 K. As can be seen in Fig. 9, the removal efficiency and adsorption uptake of Fe$_3$O$_4$@CMPFS for ARS dye was somewhat lower in real water samples (tap, lake, and pond water) compared to DI water. This can be attributed to the presence of dissolved salts, minerals, and other ionic species (e.g., Na, Cl, Mg, K, and Ca) in real water samples. These ions may compete with ARS dye molecules for active adsorption sites on the Fe$_3$O$_4$@CMPFS surface, thereby reducing the dye's access to these sites and consequently decreasing the adsorption efficiency. These results indicate that Fe$_3$O$_4$@CMPFS can be a good candidate for water remediation in different wastewater sources.
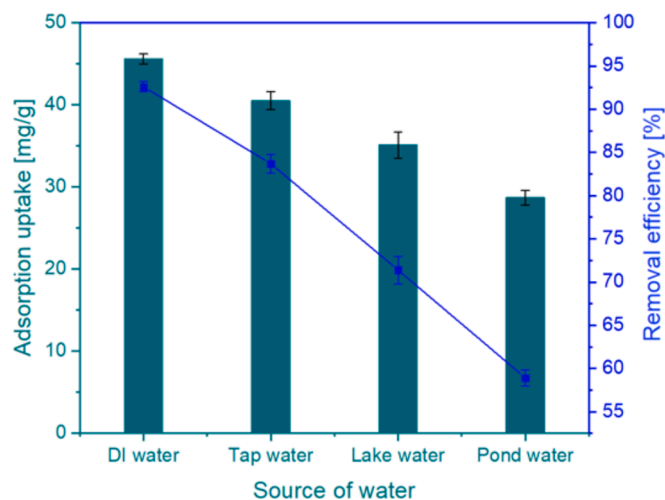
Fig. 9. The adsorption of ARS in different water samples [C_o = 50 mg/L; M = 60 mg; V = 30 mL; pH = 2.0; T = 298 K; t = 60 min; speed = 250 rpm].

4. Conclusions

The novel magnetic Fe$_3$O$_4$@CMPFS nanocomposite was successfully synthesized by the co-precipitation method. The synthesized Fe$_3$O$_4$@CMPFS was thoroughly characterized using various analytical techniques. The results from BET and VSM demonstrated that the composite possessed a high surface area (115.5 m^2/g) and exhibited favourable magnetic behaviour (Ms = 31.7 emu/g). The findings from FTIR and EDX confirmed the adsorption of ARS onto Fe$_3$O$_4$@CMPFS. The XRD results confirm that the Fe$_3$O$_4$@CMPFS composite has a crystalline structure. FE-SEM images depicted the morphology of the synthesized material before and after adsorption. To study the adsorption behaviour of ARS dye on Fe$_3$O$_4$@CMPFS, several parameters affecting ARS adsorption were investigated and discussed. The highest removal efficiency occurred in an acidic solution (pH 2.0; R% = 92.3 %). The adsorption kinetics of ARS onto the Fe$_3$O$_4$@CMPFS followed the PSO kinetic model, indicating the possible involvement of chemisorption. The isotherms best described the adsorption equilibrium data in the order Langmuir > Temkin > Freundlich > D-R model. The value of R$_L$ is 0.04, indicating favourable adsorption as it is less than 1. The thermodynamic variables $\Delta G° < 0$, $\Delta H° > 0$, and $\Delta S° > 0$ reveal that the adsorption of ARS onto Fe$_3$O$_4$@CMPFS was spontaneous and endothermic and led to an increase in the system's disorder. A thorough examination of adsorption kinetics, isotherms, and thermodynamics explained the essential roles of both chemical and physical interactions in the adsorption process, with physisorption predominant in the ARS dye adsorption onto Fe$_3$O$_4$@CMPFS. The activation energy (E$_a$) was 20.4 kJ/mol, supporting physisorption. The sticking probability (S*) value was less than 1, indicating the probability of the ARS dye sticking on the surface of Fe$_3$O$_4$@CMPFS. The regeneration experiments showed that the Fe$_3$O$_4$@CMPFS composite was desorbed with 0.1 M NaOH. After eight times of reusability cycles, the removal efficiency remained above 77 %, which represented a certain regeneration ability. The magnetic Fe$_3$O$_4$@CMPFS composite showed fast magnetic responsiveness and easily separated and recovered after adsorption. The mechanism of ARS adsorption was confirming electrostatic interactions between ARS dye and Fe$_3$O$_4$@CMPFS. These results demonstrated that Fe$_3$O$_4$@CMPFS nanocomposite is a practical, affordable, and stable adsorbent for removing ARS dye from contaminated water.

CRediT authorship contribution statement

Venkata Subbaiah Munagapati: Writing – original draft, Visualization, Methodology, Formal analysis, Data curation, Conceptualization. **Hsin-Yu Wen:** Visualization, Validation, Conceptualization. **Anjani R.K. Gollakota:** Formal analysis, Data curation, Conceptualization. **Jet-Chau Wen:** Writing – review & editing, Supervision, Resources, Funding acquisition, Data curation, Conceptualization. **Kun-Yi Andrew Lin:** Writing – review & editing, Visualization, Data curation. **Chi-Min Shu:** Visualization, Conceptualization. **Vijaya Yarramuthi:** Visualization, Validation, Conceptualization. **Praveen Kumar Basivi:** Formal analysis. **Chang Woo Kim:** Conceptualization. **Jeung-Tai Tang:** Conceptualization.

Declaration of competing interest

The authors declare that they have no known competing financial interests or personal relationships that could have appeared to influence the work reported in this paper.

Data availability

Data will be made available on request.

Acknowledgements

Appendix A. Supplementary data

Supplementary data to this article can be found online at https://doi.org/10.1016/j.molliq.2024.126197.

References

[1] P.E. Ohale, K. Chukwudi, J.N. Ndive, M.E. Michael, M.N. Abonyi, M.M. Chukwu, C.C. Obi, C.E. Onu, C.A. Igwegbe, C.O. Azie, Optimization of Fe$_2$O$_3$@BC-KC composite preparation for adsorption of Alizarin red S dye: characterization, kinetics, equilibrium, and thermodynamic studies, Results Surf. Interfaces 13 (2023) 100157, https://doi.org/10.1016/j.rsurfi.2023.100157.

[2] Y. Dong Liang, Y. Jun He, Y. Hang Zhang, Q. Qian Zhu, Adsorption property of alizarin red S by NiFe$_2$O$_4$/polyaniline magnetic composite, J. Environ. Chem. Eng. 6 (2018) 416–425, https://doi.org/10.1016/j.jece.2017.12.022.

[3] J. Wu, L. Ma, Y. Chen, Y. Cheng, Y. Liu, X. Zha, Catalytic ozonation of organic pollutants from bio-treated dyeing and finishing wastewater using recycled waste iron shavings as a catalyst: removal and pathways, Water Res. 92 (2016) 140–148, https://doi.org/10.1016/j.watres.2016.01.053.

[4] F. Rezaei, G. Moussavi, A.R. Bakhtiari, Y. Yamini, Toluene removal from waste air stream by the catalytic ozonation process with MgO/GAC composite as catalyst, J. Hazard. Mater. 306 (2016) 348–358, https://doi.org/10.1016/j.jhazmat.2015.11.026.

[5] M. Bitenc, B. Horvat, B.Ž. Likozar, G. Dražić, Z.C. Orel, The impact of ZnO load, stability and morphology on the kinetics of the photocatalytic degradation of caffeine and resazurin, Appl. Catal. B Environ. 136–137 (2013) 202–209, https://doi.org/10.1016/j.apcatb.2013.02.016.

[6] A. Turcanu, T. Bechtold, Cathodic decolourisation of reactive dyes in model effluents released from textile dyeing, J. Clean. Prod. 142 (2017) 1397–1405, https://doi.org/10.1016/j.jclepro.2016.11.167.

[7] T.H. Kim, C. Park, J. Yang, S. Kim, Comparison of disperse and reactive dye removals by chemical coagulation and Fenton oxidation, J. Hazard. Mater. 112 (2004) 95–103, https://doi.org/10.1016/j.jhazmat.2004.04.008.

[8] U. Habiba, T.A. Siddique, T.C. Joo, A. Salleh, B.C. Ang, A.M. Afifi, Synthesis of chitosan/polyvinyl alcohol/zeolite composite for removal of methyl orange, Congo red and chromium(VI) by flocculation/adsorption, Carbohydr. Polym. 157 (2017) 1568–1576, https://doi.org/10.1016/j.carbpol.2016.11.037.

[9] H. Lade, S. Govindwar, D. Paul, Mineralization and detoxification of the carcinogenic azo dye Congo red and real textile effluent by a polyurethane foam immobilized microbial consortium in an upflow column bioreactor, Int. J. Environ. Res. Public Health 12 (2015) 6894–6918, https://doi.org/10.3390/ijerph120606894.

[10] S.M. Ibrahim, A.F. Al-Hossainy, B. Saha, M.A. El-Aal, Removal of bromothymol blue dye by the oxidation method using KMnO$_4$: accelerating the oxidation reaction by Ru (III) catalyst, J. Mol. Struct. 1268 (2022) 133679, https://doi.org/10.1016/j.molstruc.2022.133679.

[11] N. Mameda, H. Park, K.H. Choo, Electrochemical filtration process for simultaneous removal of refractory organic and particulate contaminants from wastewater effluents, Water Res. 144 (2018) 699–708, https://doi.org/10.1016/j.watres.2018.08.003.

[12] F. Al-Badaii, K.M. Jansar, N.A.A. Jalil, A.A. Halim, Sustainable boron removal from aqueous solutions using pomegranate peel adsorbents: a comprehensive study on isotherms, kinetics, and thermodynamics, Desalin. Water Treat. 317 (2024) 100045, https://doi.org/10.1016/j.dwt.2024.100045.

[13] M. Kamranifar, M. Khodadadi, V. Samiei, B. Dehdashti, M. Noori Sepehr, L. Rafati, N. Nasseh, Comparison the removal of reactive red 195 dye using powder and ash of barberry stem as a low cost adsorbent from aqueous solutions: isotherm and kinetic study, J. Mol. Liq. 255 (2018) 572–577, https://doi.org/10.1016/j.molliq.2018.01.188.

[14] N.K. Soliman, A.F. Moustafa, A.A. Aboud, K.S.A. Halim, Effective utilization of Moringa seeds waste as a new green environmental adsorbent for removal of industrial toxic dyes, J. Mater. Res. Technol. 8 (2019) 1798–1808, https://doi.org/10.1016/j.jmrt.2018.12.010.

[15] V.S. Munagapati, V. Yarramuthi, Y. Kim, K.M. Lee, D.S. Kim, Removal of anionic dyes (Reactive Black 5 and Congo Red) from aqueous solutions using Banana Peel Powder as an adsorbent, Ecotoxicol. Environ. Saf. 148 (2018) 601–607, https://doi.org/10.1016/j.ecoenv.2017.10.075.

[16] C. Bhattacharjee, S. Dutta, V.K. Saxena, A review on biosorptive removal of dyes and heavy metals from wastewater using watermelon rind as biosorbent, Environ. Adv. 2 (2020) 100007, https://doi.org/10.1016/j.envadv.2020.100007.

[17] M. Tukaram Bai, O. Shaik, J. Kavitha, M.S. Hemanth Varma, N. Chittibabu, Biosorption of eosin yellow dye from aqueous solution using sugarcane bagasse: equillibrium, kinetics and thermodynamics, Mater. Today Proc. 26 (2019) 842–849, https://doi.org/10.1016/j.matpr.2020.01.051.

[18] S. Kainth, P. Sharma, O.P. Pandey, Green sorbents from agricultural wastes: a review of sustainable adsorption materials, Appl. Surf. Sci. Adv. 19 (2024) 100562, https://doi.org/10.1016/j.apsadv.2023.100562.

[19] M. Touihri, F. Guesmi, C. Hannachi, B. Hamrouni, L. Sellaoui, M. Badawi, J. Poch, N. Fiol, Single and simultaneous adsorption of Cr(VI) and Cu (II) on a novel Fe3O4/pine cones gel beads nanocomposite: experiments, characterization and isotherms modeling, Chem. Eng. J. 416 (2021) 129101, https://doi.org/10.1016/j.cej.2021.129101.

[20] A. Saravanan, S. Karishma, S. Jeevanantham, S. Jeyasri, A.R. Kiruthika, P. S. Kumar, P.R. Yaashikaa, Optimization and modeling of reactive yellow adsorption by surface modified Delonix regia seed: study of nonlinear isotherm and kinetic parameters, Surf. Interfaces 20 (2020) 100520, https://doi.org/10.1016/j.surfin.2020.100520.

[21] V.S. Munagapati, J.C. Wen, C.L. Pan, Y. Gutha, J.H. Wen, Enhanced adsorption performance of Reactive Red 120 azo dye from aqueous solution using quaternary amine modified orange peel powder, J. Mol. Liq. 285 (2019) 375–385, https://doi.org/10.1016/j.molliq.2019.04.081.

[22] Y.L.D.O. Salomón, J. Georgin, D.S.P. Franco, M.S. Netto, D.G.A. Piccilli, E. L. Foletto, L.F.S. Oliveira, G.L. Dotto, High-performance removal of 2,4-dichlorophenoxyacetic acid herbicide in water using activated carbon derived from Queen palm fruit endocarp (Syagrus romanzoffiana), J. Environ. Chem. Eng. 9 (2021) 104911, https://doi.org/10.1016/j.jece.2020.104911.

[23] S. Debnath, N. Ballav, A. Maity, K. Pillay, Competitive adsorption of ternary dye mixture using pine cone powder modified with β-cyclodextrin, J. Mol. Liq. 225 (2017) 679–688, https://doi.org/10.1016/j.molliq.2016.10.109.

[24] R. Widiartyasari Prihatdini, A. Suratman, D. Siswanta, Linear and nonlinear modeling of kinetics and isotherm of malachite green dye adsorption to trimellitic-modified pineapple peel, Mater. Today Proc. 88 (2023) 33–40, https://doi.org/10.1016/j.matpr.2023.07.108.

[25] M. Ahmed, F. Mashkoor, A. Nasar, Development, characterization, and utilization of magnetized orange peel waste as a novel adsorbent for the confiscation of crystal violet dye from aqueous solution, Groundw. Sustain. Dev. 10 (2020) 100322, https://doi.org/10.1016/j.gsd.2019.100322.

[26] N. Alizadeh, S. Shariati, N. Besharati, Adsorption of crystal violet and methylene blue on azolla and fig leaves modified with magnetite iron oxide nanoparticles, Int. J. Environ. Res. 11 (2017) 197–206, https://doi.org/10.1007/s41742-017-0019-1.

[27] V. Subbaiah Munagapati, H.Y. Wen, A.R.K. Gollakota, J.C. Wen, C.M. Shu, K. Y. Andrew Lin, V. Yarramuthi, J.H. Wen, G. Mallikarjuna Reddy, G.V. Zyryanov, Enhanced removal of anionic Methyl orange azo dye by an iron oxide (Fe3O4) loaded lotus leaf powder (LLP@Fe3O4) composite: synthesis, characterization, kinetics, isotherms, and thermodynamic perspectives, Inorg. Chem. Commun. 151 (2023) 110625, https://doi.org/10.1016/j.inoche.2023.110625.

[28] V. Subbaiah Munagapati, H.Y. Wen, A.R.K. Gollakota, J.C. Wen, C.M. Shu, K. Y. Andrew Lin, Z. Tian, J.H. Wen, G. Mallikarjuna Reddy, G.V. Zyryanov, Magnetic Fe3O4 nanoparticles loaded papaya (Carica papaya L.) seed powder as an effective and recyclable adsorbent material for the separation of anionic azo dye (Congo Red) from liquid phase: evaluation of adsorption properties, J. Mol. Liq. 345 (2022) 118255, https://doi.org/10.1016/j.molliq.2021.118255.

[29] G. Mohini, J.K. Sahoo, S.K. Sahoo, C. Bharati, M. Acharya, Optimisation and evaluation of reactive eriochrome black T dye removal on magnetic iron modified with sky fruit from an aqueous solution, Indian Chem. Eng. 66 (2024) 117–140, https://doi.org/10.1080/00194506.2023.2280695.

[30] P. Panneerselvam, N. Morad, K.A. Tan, R. Mathiyarasi, Removal of Rhodamine B dye using activated carbon prepared from Palm Kernel Shell and coated with iron oxide nanoparticles, Sep. Sci. Technol. 47 (2012) 742–752, https://doi.org/10.1080/01496395.2011.625069.

[31] A. Stavrinou, C.A. Aggelopoulos, C.D. Tsakiroglou, Exploring the adsorption mechanisms of cationic and anionic dyes onto agricultural waste peels of banana, cucumber and potato: adsorption kinetics and equilibrium isotherms as a tool, J. Environ. Chem. Eng. 6 (2018) 6958–6970, https://doi.org/10.1016/j.jece.2018.10.063.

[32] M.J. Sharifi, A. Nouralishahi, A. Hallajisani, Fe3O4-chitosan nanocomposite as a magnetic biosorbent for removal of nickel and cobalt heavy metals from polluted water, Int. J. Biol. Macromol. 248 (2023) 125984, https://doi.org/10.1016/j.ijbiomac.2023.125984.

[33] M. Yuan, D. Liu, S. Shang, Z. Song, Q. You, L. Huang, S. Cui, A novel magnetic Fe3O4/cellulose nanofiber/polyethyleneimine/thiol-modified montmorillonite aerogel for efficient removal of heavy metal ions: adsorption behavior and mechanism study, Int. J. Biol. Macromol. 253 (2023) 126634, https://doi.org/10.1016/j.ijbiomac.2023.126634.

[34] A. Kumar Prajapati, M. Kumar Mondal, Green synthesis of Fe3O4-onion peel biochar nanocomposites for adsorption of Cr(VI), methylene blue and congo red dye from aqueous solutions, J. Mol. Liq. 349 (2022) 118161, https://doi.org/10.1016/j.molliq.2021.118161.

[35] V. Eyupoglu, A. Aksu, H.F. Çetinkaya, H.İ. Çetintaş, S. Çetinkaya, B. Tüzün, Biosorption of dye crystal violet on Tragopogon sp. leaf powder: Equilibrium, kinetics, thermodynamics, and DFT calculations, J. Mol. Liq. 398 (2024) 124226, https://doi.org/10.1016/j.molliq.2024.124226.

[36] S. Rajoriya, V.K. Saharan, A.S. Pundir, M. Nigam, K. Roy, Adsorption of methyl red dye from aqueous solution onto eggshell waste material: kinetics, isotherms and thermodynamic studies, Curr. Res. Green Sustain. Chem. 4 (2021) 100180, https://doi.org/10.1016/j.crgsc.2021.100180.

[37] M. Masuku, J.F. Nure, H.I. Atagana, N. Hlongwa, T.T.I. Nkambule, Pinecone biochar for the Adsorption of chromium (VI) from wastewater: kinetics, thermodynamics, and adsorbent regeneration, Environ. Res. 258 (2024) 119423, https://doi.org/10.1016/j.envres.2024.119423.

[38] V.S. Rana, N. Sharma, Adsorption profile of anionic and cationic dyes through Fe3O4 embedded oxidized Sterculia gum/Gelatin hybrid gel matrix, Int. J. Biol. Macromol. 232 (2023) 123098, https://doi.org/10.1016/j.ijbiomac.2022.12.317.

[39] N. Amiralian, M. Mustapic, M.S.A. Hossain, C. Wang, M. Konarova, J. Tang, J. Na, A. Khan, A. Rowan, Magnetic nanocellulose: a potential material for removal of dye from water, J. Hazard. Mater. 394 (2020) 122571, https://doi.org/10.1016/j.jhazmat.2020.122571.

[40] A. Hota, S.G.K. Patro, S.K. Panda, M.A. Khan, M.A. Hasan, S. Islam, M. Alsubih, N. A. Khan, S. Zahmatkesh, Removing fluoride ions from wastewater by Fe3O4 nanoparticles: modified Rhodophytes (red algae) as biochar, J. Water Process Eng. 58 (2024) 104776, https://doi.org/10.1016/j.jwpe.2024.104776.

[41] A.K. Behera, K.P. Shadangi, P.K. Sarangi, Efficient removal of Rhodamine B dye using biochar as an adsorbent: study the performance, kinetics, thermodynamics, adsorption isotherms and its reusability, Chemosphere 354 (2024) 141702, https://doi.org/10.1016/j.chemosphere.2024.141702.

[42] S. Aravindhan, G. Bharath Kumar, M. Saravanan, A. Arumugam, Delonix regia biomass as an eco-friendly biosorbent for effective Alizarin Red S textile dye removal: characterization, kinetics, and isotherm studies, Bioresour. Technol. Reports 25 (2024) 101721, https://doi.org/10.1016/j.biteb.2023.101721.

[43] N.S. Al-Kadhi, G.M. Al-Senani, F.K. Algethami, R.K. Shah, F.A. Saad, K. ur Rehman, L. Khezami, E.A. Abdelrahman, Facile synthesis of MgO/ZnO nanocomposite for efficient removal of alizarin red S dye from aqueous media, Inorg. Chem. Commun. 162 (2024) 112233, https://doi.org/10.1016/j.inoche.2024.112233.

[44] D. Brahma, H. Nath, D. Borah, M. Debnath, H. Saikia, Coconut husk ash fabricated CoAl-layered double hydroxide composite for the enhanced sorption of malachite green dye: isotherm, kinetics and thermodynamic studies, Inorg. Chem. Commun. 144 (2022) 109878, https://doi.org/10.1016/j.inoche.2022.109878.

[45] J.S. Algethami, M.A.M. Alhamami, A.A. Alqadami, S. Melhi, A.F. Seliem, Magnetic hydrochar grafted-chitosan for enhanced efficient adsorption of malachite green dye from aqueous solutions: modeling, adsorption behavior, and mechanism analysis, Int. J. Biol. Macromol. 254 (2024) 127767, https://doi.org/10.1016/j.ijbiomac.2023.127767.

[46] M. Asif Tahir, H.N. Bhatti, M. Iqbal, Solar red and brittle blue direct dyes adsorption onto eucalyptus angophoroides bark: equilibrium, kinetics and thermodynamic studies, J. Environ. Chem. Eng. 4 (2016) 2431–2439, https://doi.org/10.1016/j.jece.2016.04.020.

[47] M. Noori, M. Tahmasebpoor, R. Foroutan, Enhanced adsorption capacity of low-cost magnetic clinoptilolite powders/beads for the effective removal of methylene blue: adsorption and desorption studies, Mater. Chem. Phys. 278 (2022) 125655, https://doi.org/10.1016/j.matchemphys.2021.125655.

[48] H.M. Abumelha, Enhancing brilliant green dye removal via bio composite chitosan and food-grade algae capsulated ruthenium metal-organic framework: optimization of adsorption parameters by box-behnken design, Int. J. Biol. Macromol. 264 (2024) 130635, https://doi.org/10.1016/j.ijbiomac.2024.130635.

[49] B. Tanhaei, A. Ayati, M. Sillanpää, Magnetic xanthate modified chitosan as an emerging adsorbent for cationic azo dyes removal: kinetic, thermodynamic and isothermal studies, Int. J. Biol. Macromol. 121 (2019) 1126–1134, https://doi.org/10.1016/j.ijbiomac.2018.10.137.

[50] A.R.K. Gollakota, V.S. Munagapati, V. Volli, S. Gautam, J.C. Wen, C.M. Shu, Coal bottom ash derived zeolite (SSZ-13) for the sorption of synthetic anion Alizarin Red S (ARS) dye, J. Hazard. Mater. 416 (2021) 125925, https://doi.org/10.1016/j.jhazmat.2021.125925.

[51] M.B. Gholivand, Y. Yamini, M. Dayeni, S. Seidi, E. Tahmasebi, Adsorptive removal of alizarin red-S and alizarin yellow GG from aqueous solutions using polypyrrole-coated magnetic nanoparticles, J. Environ. Chem. Eng. 3 (2015) 529–540, https://doi.org/10.1016/j.jece.2015.01.011.

[52] A.A. Nayl, A.I. Abd-Elhamid, I.M. Ahmed, S. Brase, Preparation and characterization of magnetite talc (Fe3O4@Talc) nanocomposite as an effective adsorbent for Cr(VI) and Alizarin Red S dye, Materials 15 (2022) 3401, https://doi.org/10.3390/ma15093401.

[53] R. Nodehi, H. Shayesteh, A. Rahbar-Kelishami, Fe₃O₄@NiO core–shell magnetic nanoparticle for highly efficient removal of Alizarin red S anionic dye, Int. J. Environ. Sci. Technol. 19 (2022) 2899–2912, https://doi.org/10.1007/s13762-021-03399-8.

[54] Z. Zhang, H. Chen, W. Wu, W. Pang, G. Yan, Efficient removal of Alizarin Red S from aqueous solution by polyethyleneimine functionalized magnetic carbon nanotubes, Bioresour. Technol. 293 (2019) 122100, https://doi.org/10.1016/j.biortech.2019.122100.

[55] M. Fayazi, M. Ghanei-Motlagh, M.A. Taher, The adsorption of basic dye (Alizarin red S) from aqueous solution onto activated carbon/γ-Fe₂O₃ nano-composite: kinetic and equilibrium studies, Mater. Sci. Semicond. Process. 40 (2015) 35–43, https://doi.org/10.1016/j.mssp.2015.06.044.

[56] N. Ali, F. Ali, I. Ullah, Z. Ali, L. Duclaux, L. Reinert, J.M. Lévêque, A. Farooq, M. Bilal, I. Ahmad, Organically modified micron-sized vermiculite and silica for efficient removal of Alizarin Red S dye pollutant from aqueous solution, Environ. Technol. Innov. 19 (2020) 101001, https://doi.org/10.1016/j.eti.2020.101001.

[57] F.M. Machado, S.A. Carmalin, E.C. Lima, S.L.P. Dias, L.D.T. Prola, C. Saucier, I. M. Jauris, I. Zanella, S.B. Fagan, Adsorption of Alizarin Red S dye by carbon nanotubes: an experimental and theoretical investigation, J. Phys. Chem. C 120 (2016) 18296–18306, https://doi.org/10.1021/acs.jpcc.6b03884.

[58] M. Bellaj, H. Yazid, K. Aziz, A. Regti, M. El Haddad, M. El Achaby, A. Abourriche, L. Gebrati, T.A. Kurniawan, F. Aziz, Eco-friendly synthesis of clay-chitosan composite for efficient removal of alizarin red S dye from wastewater: a comprehensive experimental and theoretical investigation, Environ. Res. 247 (2024) 118352, https://doi.org/10.1016/j.envres.2024.118352.

[59] B. Sowjanya, U. Sirisha, A. Suhasini Juttuka, S. Matla, P. King, M. Vangalapati, Synthesis and characterization of zinc oxide nanoparticles: it's application for the removal of alizarin red S dye, Mater. Today Proc. 62 (2022) 3968–3972, https://doi.org/10.1016/j.matpr.2022.04.576.

[60] S. Solanki, S. Sinha, C.S. Seth, S. Tyagi, A. Goyal, R. Singh, Enhanced adsorption of Bismark Brown R dye by chitosan conjugated magnetic pectin loaded filter mud: a comprehensive study on modeling and mechanisms, Int. J. Biol. Macromol. 270 (2024) 131987, https://doi.org/10.1016/j.ijbiomac.2024.131987.

[61] T.C. Egbosiuba, T.Q. Tran, K. Arole, Y. Zhang, C.E. Enyoh, S. Mustapha, J.O. Tijani, V.K. Yadav, V.C. Anadebe, A.S. Abdulkareem, Biotreatment of clay-based adsorbent to eliminate arsenic (V) ions and malachite green from wastewater: isotherm, kinetics, thermodynamics, reusability and mechanism, Results Eng. 22 (2024) 102073, https://doi.org/10.1016/j.rineng.2024.102073.

[62] E.K. Owino, V.O. Shikuku, W.N. Nyairo, C.O. Kowenje, B. Otieno, Valorization of solid waste incinerator fly ash by geopolymer production for removal of anionic bromocresol green dye from water: kinetics, isotherms and thermodynamics studies, Sustain. Chem. Environ. 3 (2023) 100026, https://doi.org/10.1016/j.scenv.2023.100026.

[63] A.M. Omer, W. Abdel-Alim Sadik, R.A. Elady, T.M. Tamer, M.M. Abd-Ellatif, M. S. Mohy-Eldin, Novel amino-ethyl carboxymethyl cellulose crosslinked ampholyte hydrogel development for Methyl Orange Removal from Waste water: kinetics, isotherms, and thermodynamics studies, Desalin. Water Treat. 317 (2024) 100041, https://doi.org/10.1016/j.dwt.2024.100041.

[64] S. Chen, C. Qin, T. Wang, F. Chen, X. Li, H. Hou, M. Zhou, Study on the adsorption of dyestuffs with different properties by sludge-rice husk biochar: adsorption capacity, isotherm, kinetic, thermodynamics and mechanism, J. Mol. Liq. 285 (2019) 62–74, https://doi.org/10.1016/j.molliq.2019.04.035.

[65] H.R. Mahmoud, S.M. Ibrahim, S.A. El-Molla, Textile dye removal from aqueous solutions using cheap MgO nanomaterials: adsorption kinetics, isotherm studies and thermodynamics, Adv. Powder Technol. 27 (2016) 223–231, https://doi.org/10.1016/j.apt.2015.12.006.